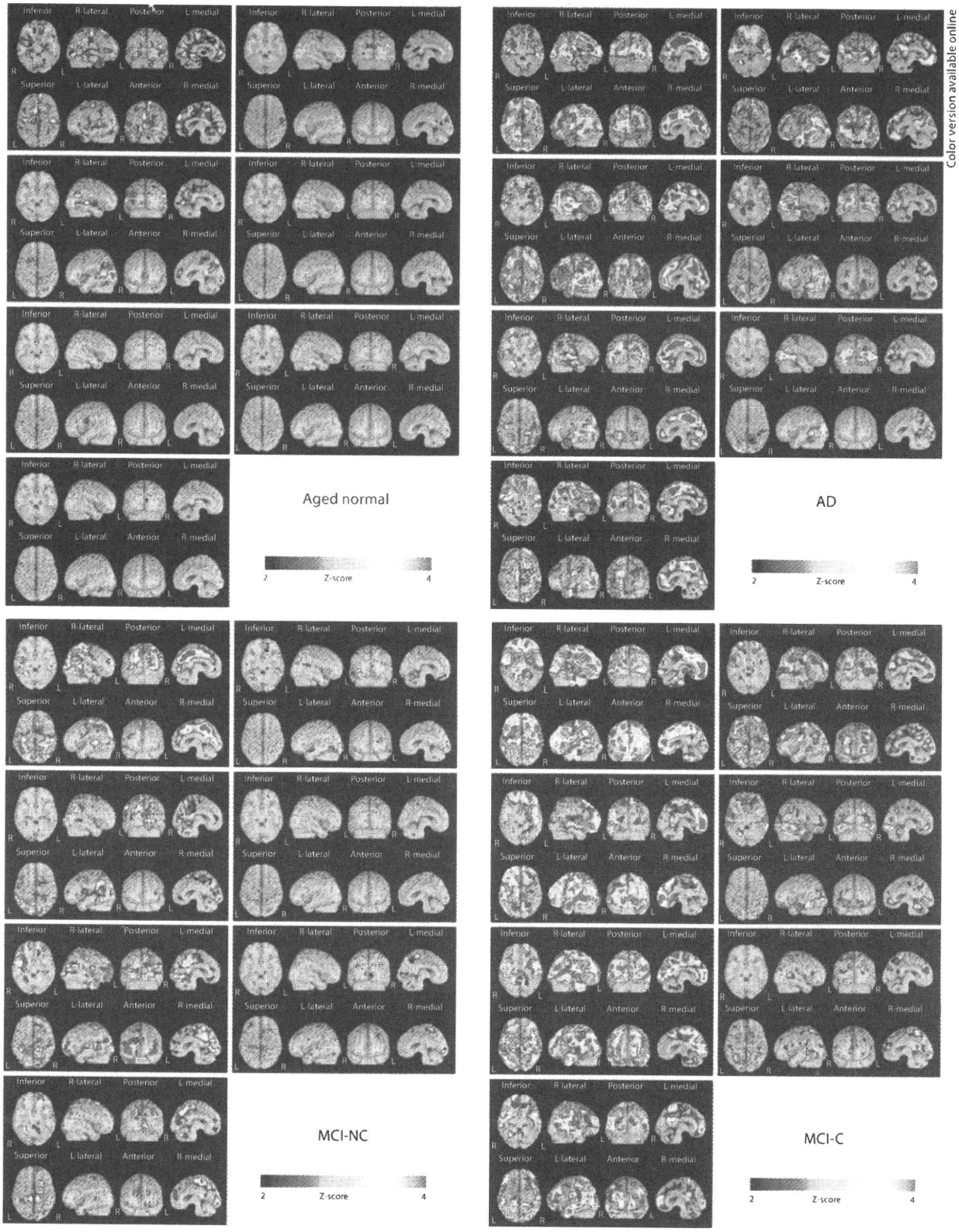

Color version available online

Table 4. Average SUVR between 20 and 40 min after injection

	SUVR					Cohen's d	
	aged normal	MCI-NC	MCI-C	AD1	AD2	MCI-NC and MCI-C	aged normal and all AD
Frontal	0.98 ± 0.05	0.98 ± 0.06	1.11 ± 0.10*,#	1.08 ± 0.08*	1.06 ± 0.05	1.62	1.69
Temporal	1.02 ± 0.04	1.06 ± 0.07	1.18 ± 0.07*,#	1.18 ± 0.07*,#	1.18 ± 0.06*,#	1.7	2.93
Parietal	1.06 ± 0.04	1.08 ± 0.05	1.17 ± 0.05*	1.18 ± 0.06*,#	1.19 ± 0.09*	1.76	2.25
Occipital	1.05 ± 0.04	1.09 ± 0.06	1.11 ± 0.06	1.13 ± 0.07*	1.13 ± 0.05*	0.37	1.51
Posterior cingulate	1.11 ± 0.07	1.12 ± 0.07	1.19 ± 0.10	1.20 ± 0.09	1.22 ± 0.05*	0.85	1.51

Values denote means ± SD. * $p < 0.05$ versus aged normal group; # $p < 0.05$ versus MCI-NC group.

tal cortex. In the temporal cortex, the number of positively stained Aβ plaques showed a significantly positive correlation with the number of dense- and diffuse-type plaques. However, in the frontal cortex, the number of positively stained Aβ plaques showed a significant correlation with only the number of dense-type plaques and not with the number of diffuse-type plaques (fig. 6).

Discussion

The identification of patients with a high risk of developing AD in the MCI stage is of great clinical value. However, it is difficult to predict the conversion from MCI to AD from a clinical and neuropsychological perspective. In comparison with MRI and CT, PET is relatively expensive and not accessible. Consequently, PET is not routinely used in the diagnosis of AD. However, PET imaging provides useful diagnostic information for predicting conversion from MCI to AD when MRI fails to provide sufficient information [15]. A recent Pittsburgh compound B (PiB) PET study demonstrated that in vivo detection of amyloid deposition provides useful prognostic information in MCI [19]. The present study using BF-227 PET showed similar predictive performance to previous PiB PET results although the signal-to-background ratio increase for BF-227 in patients with AD over controls was considerably lower than that for PiB. The lower signal-to-background ratio of BF-227 would be due to the lower detection sensitivity of BF-227 than that of PiB for diffuse plaques. However, BF-227 PET may have a better predictive value for progression from MCI to AD than PiB PET because the deposition of diffuse plaque is observed even during the normal aging process. A head-to-head comparison of BF-227 PET with PiB PET will clarify which tracer has more predictive power for conversion of MCI to AD.

Voxel-based analysis of PET images allows an objective and sensitive identification of regional change in uptake of the tracer. BF-227 is a PET tracer that binds to amyloid plaques in the brain [10]. Although BF-227 binds well to amyloid fibrils in vitro, the signal-to-background ratio for [^{11}C]BF-227 PET images was relatively lower than that for PiB PET, possibly due to the lower binding affinity of BF-227 to Aβ fibrils compared to PiB. This drawback can be overcome by voxel-based statistical comparison with a normal control database. In fact, the abnormal distribution of [^{11}C]BF-227 in MCI-C was more clearly demonstrated by Z-score mapping analysis than by unprocessed SUVR images. In addition, a portion of MCI-NC showed a high Z-score in the posterior neocortical areas, which may reflect early Aβ pathology in the brain. The pathological significance of these abnormalities will be elucidated after having followed up these patients.

A commonly observed feature in the Z-score maps of MCI-C and patients with AD was the change in bilateral temporal and temporooccipital cortices, which was also detected by between-group comparison with the aged

Fig. 2. a Voxel-by-voxel Z-score analysis of [^{11}C]BF-227 PET images for aged normal subjects (left) and patients with AD (right) with the mean and SD of PET images of 15 normal controls. The Z-score maps were displayed by the surface projection of the spatially normalized MR image. **b** Voxel-by-voxel Z-score analysis by comparison of [^{11}C]BF-227 PET images for MCI-NC (left) and MCI-C (right) with the mean and SD of PET images of 15 normal controls. The Z-score maps were displayed by the surface projection of the spatially normalized MR image.

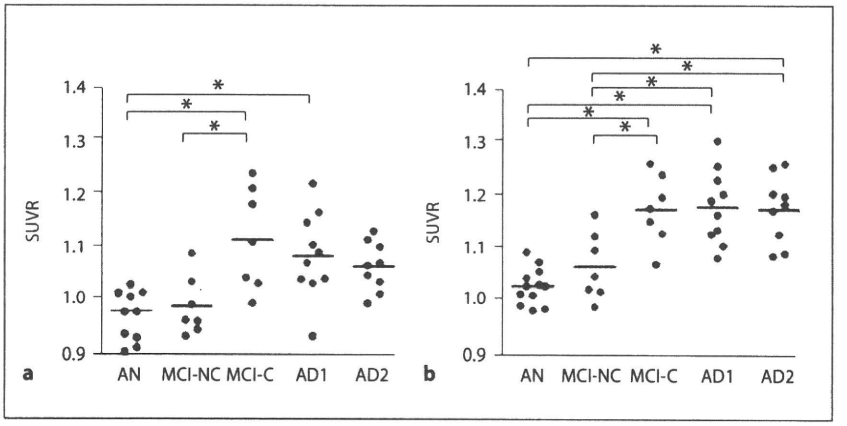

Fig. 3. Regional BF-227 SUVR in the frontal (**a**) and temporal (**b**) cortices. Horizontal bar: average SUVR in each group. * $p < 0.05$.

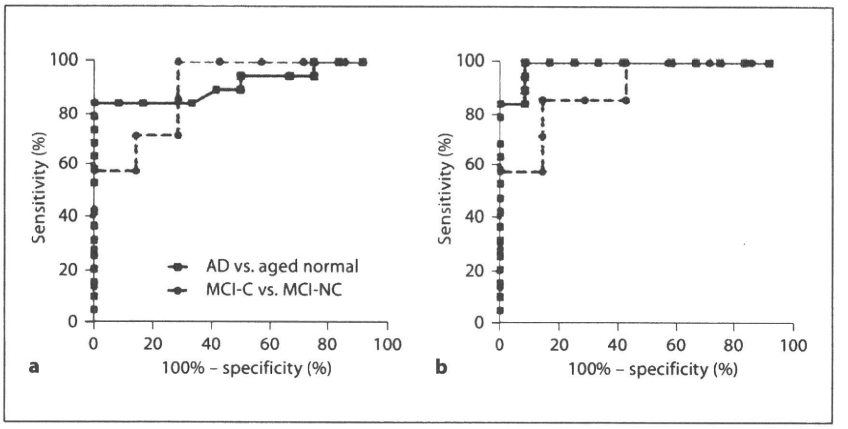

Fig. 4. ROC curves of regional BF-227 SUVR in the frontal (**a**) and temporal (**b**) cortices for differentiation between patients with AD and aged normal controls (solid line) and between MCI-C and MCI-NC (dashed line).

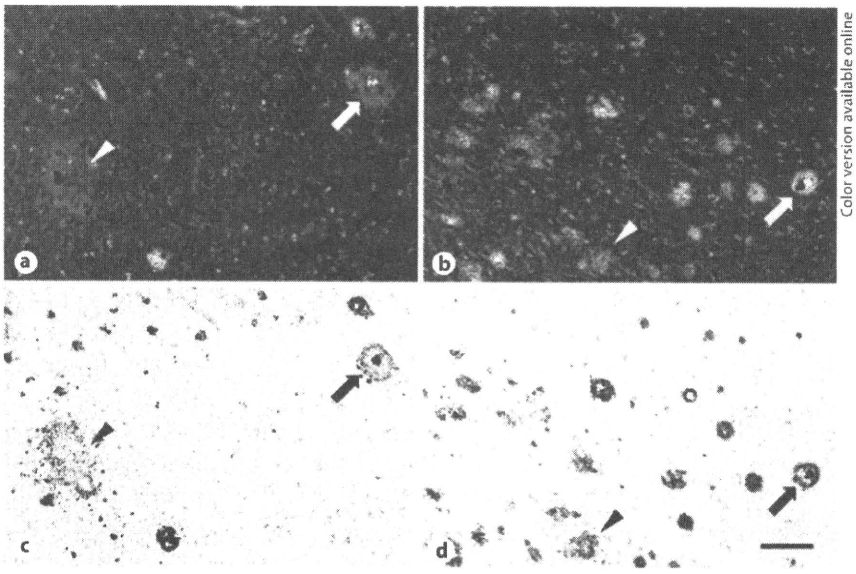

Fig. 5. Neuropathologic staining of AD frontal (**a**, **c**) and temporal (**b**, **d**) brain sections by BF-227. Cored plaques (arrows) are clearly stained with BF-227 (**a**, **b**). Cored-plaque staining with BF-227 correlates well with Aβ immunostaining in adjacent sections (**c**, **d**). Diffuse plaques (arrowheads) are faintly stained with BF-227 in the frontal brain section (**a**), but moderately stained in the temporal brain section (**b**). Scale bar = 100 μm.

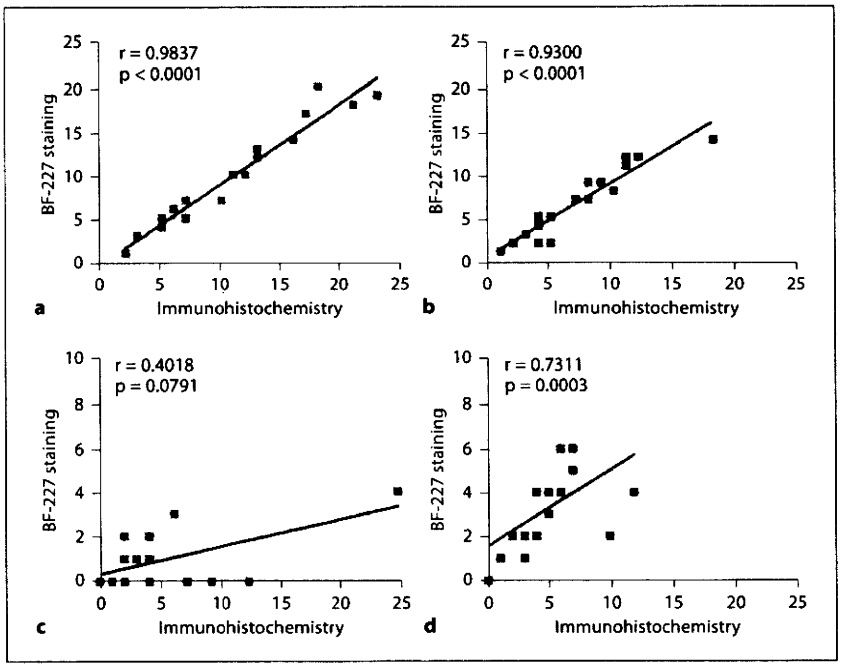

Fig. 6. Correlations between the numbers per unit area of amyloid plaques stained with Aβ-specific antibody and BF-227. The density of dense-type plaques showed a significant correlation with positive staining with BF-227 both in the frontal (**a**) and temporal (**b**) brain sections. However, the density of diffuse-type plaques was not correlated with BF-227 staining in the frontal cortex (**c**), and weakly correlated with BF-227 staining in the temporal cortex (**d**).

normal controls using the SPM software. The preferential [^{11}C]BF-227 retention in the posterior neocortical region corresponded with an area containing a high density of neuritic plaques [20]. This finding was confirmed by our analysis using postmortem AD brain samples. From these findings, the amount of dense plaque deposits in the posterior neocortical region, which could be measured by [^{11}C]BF-227 PET, is a reliable index of prognosis in patients with MCI. Interestingly, the Z-score mapping of BF-227 PET images further elucidated individual variation in the regional distribution of amyloid plaque deposition in patients with AD. There is great interest in determining the relationship between this heterogeneity and the clinical phenotype of patients with AD, which should be investigated in the future with data from a larger population. About 2/3 of patients with AD showed elevated BF-227 uptake in both anterior and posterior association areas, and the remaining 1/3 showed posterior-oriented BF-227 uptake. However, none of the patients with AD showed frontal-oriented BF-227 uptake. Although our analysis has been cross-sectional, these findings suggest that neuritic plaque deposition in AD starts at the posterior association areas and then spreads to other brain regions during AD progression.

The relatively lower [^{11}C]BF-227 retention in the frontal cortex of patients in the AD group may be a chance finding due to the small sample size. However, previous analysis of postmortem AD brain samples indicated that a majority of neocortical plaques start as fibrillar Aβ deposits and, in the late stages of AD, shift to nonfibrillar plaques [21]. Therefore, the relatively lower [^{11}C]BF-227 uptake in the AD group may be due to the transformation of fibrillar Aβ deposits to nonfibrillar Aβ deposits during AD progression. A longitudinal evaluation of [^{11}C]BF-227 uptake is necessary to examine whether the neocortical Aβ deposits reflected by BF-227 uptake change during the course of AD progression. In addition, the quantitative analysis of BF-227 binding to amyloid plaques should be performed in the future to eliminate the influence of regional cerebral hypoperfusion.

The definitive diagnosis of AD depends on postmortem examination because histological analysis of tissue samples is the only method for assessing AD pathology with certainty [7, 22]. Senile plaques were classified on the basis of the morphology of histopathological staining: diffuse plaques, primitive plaques, classical plaques and compacted plaques [23]. The diffuse plaques were abundant in healthy controls, whereas mature plaques such as primitive, classical and compact ones were typical in patients with AD. In our study, strong correlations between the number of mature plaques and BF-227 binding in the frontal and temporal cortices were observed. Further-

more, the temporal cortex exhibited a significant correlation between the number of diffuse-type plaques and BF-227 binding. However, the frontal cortex showed no such correlation. Generally, primitive, classical and compact plaques contain more amyloid fibrils than diffuse plaques. A previous electron microscopic examination has suggested that diffuse plaques in the frontal cortex contain a small amount of amyloid fibrils and do not easily transform to primitive plaques, while those in the temporal cortex contain more amyloid fibrils and tend to transform to primitive plaques [24]. Therefore, the binding ability of BF-227 to different types of diffuse plaques in the frontal and temporal cortices partly explains why BF-227 tends to accumulate in the temporal cortex of the AD brain. In addition, the density of dense-type plaques in the temporal cortex was higher than that in the frontal cortex in our analysis. This finding is in accordance with another comprehensive neuropathological examination that showed a higher density of amyloid plaques in the temporal cortex than in the frontal cortex [20, 25]. Thus, the lower density of primitive plaques in the frontal cortex may explain the relatively lower BF-227 uptake in the frontal cortex. Further analyses using more AD brain samples and radiolabeled BF-227 are required in the future because only one brain was examined in this study, and the concentration of BF-227 used to stain the postmortem tissue was not equivalent to the expected in vivo concentrations.

Previous PiB PET studies have shown the greatest tracer uptake in the precuneus and posterior cingulate cortex. However, our PET study demonstrated greater BF-227 uptake in the lateral temporal and parietal cortices of the AD brain samples than in the posterior cingulate cortex. A recent study demonstrated that the number of diffuse plaques in the posterior cingulate gyrus was greater than that in other neocortical areas. However, the number of neuritic plaques in the posterior cingulate cortex was not greater than that in other neocortical areas during AD progression [26]. Therefore, the modest posterior cingulate BF-227 uptake elevation in some patients with AD may be due to the lower binding affinity of BF-227 to diffuse plaques than that of PiB.

There are several limitations of this study. First, the sample size was small, primarily because of the limited follow-up period. Second, no repeat scans were performed to really assess changes in BF-227 uptake over time. Future studies should include longitudinal data from a larger sample. Third, the patients with MCI were older than the aged normal controls. Therefore, the higher neocortical uptake of [^{11}C]BF-227 in patients with MCI could be attributed to the effect of aging. However, no age-related change in BF-227 uptake was observed in the aged normal controls [10]. Furthermore, no significant elevation of [^{11}C]BF-227 uptake was observed in the MCI-NC group compared with that in the aged normal control group. Therefore, the higher [^{11}C]BF-227 uptake in the MCI-C group is not likely due to the effect of aging. We need to further address this issue by controlling for the age of normal controls and patients with MCI.

In summary, [^{11}C]BF-227 PET can detect the early Aβ load in the lateral temporal cortex of patients with MCI and AD. The amount of [^{11}C]BF-227 uptake in the temporal cortex was strongly related to prognosis in patients with MCI. BF-227 would be less subjective to amyloid pathology during the process of aging since this probe is believed to bind selectively to dense Aβ plaques. Thus, [^{11}C]BF-227 PET offers unique information concerning AD pathology that cannot be obtained by other PET tracers, which would be useful for the MCI population since it allows prediction of their risk for progression to AD in the near future.

Acknowledgments

This study was supported by the Health and Labor Sciences Research Grants for Translational Research from the Ministry of Health and the Grant-in-Aid for Scientific Research on Priority Areas – Integrative Brain Research from the Ministry of Education, Culture, Sports, Science, and Technology of Japan (20019006). We appreciate the technical assistance provided by Dr. S. Watanuki, Dr. Y. Ishikawa and M. Kato during the PET studies.

References

1 Glenner GG, Wong CW: Alzheimer's disease: initial report of the purification and characterization of a novel cerebrovascular amyloid protein. Biochem Biophys Res Commun 1984;120:885–890.

2 Masters CL, Multhaup G, Simms G, Pottgiesser J, Martins RN, Beyreuther K: Neuronal origin of a cerebral amyloid: neurofibrillary tangles of Alzheimer's disease contain the same protein as the amyloid of plaque core and blood vessels. EMBO J 1985;4:2757–2763.

3 Masters CL, Simms G, Weinman NA, Multhaup G, McDonald BL, Beyreuther K: Amyloid plaque core protein in Alzheimer disease and Down syndrome. Proc Natl Acad Sci USA 1985;82:4245–4249.

4 Hardy J, Selkoe DJ: The amyloid hypothesis of Alzheimer's disease: progress and problems on the road to therapeutics. Science 2002;297:353–356.

5 Petersen RC, Smith GE, Waring SC, Ivnik RJ, Tangalos EG, Kokmen E: Mild cognitive impairment: clinical characterization and outcome. Arch Neurol 1999;56:303–308.
6 Petersen RC: Mild cognitive impairment as a diagnostic entity. J Intern Med 2004;256: 183–194.
7 Ikonomovic MD, Klunk WE, Eric E, Abrahamson EE, Mathis CA, Price JC, Tsopelas ND, Lopresti BJ, Ziolko S, Bi WZ, Paljug WR, Debnath ML, Hope CE, Barbara A, Isanski BA, Hamilton RL, DeKosky ST: Post-mortem correlates of in vivo PiB-PET amyloid imaging in a typical case of Alzheimer's disease. Brain 2008;131:1630–1645.
8 Furumoto S, Okamura N, Iwata R, Yanai K, Arai H, Kudo Y: Recent advances in the development of amyloid imaging agents. Curr Top Med Chem 2007;7:1773–1789.
9 Klunk WE, Engler H, Nordberg A, Wang Y, Blomqvist G, Holt DP, Bergström M, Savitcheva I, Huang GF, Estrada S, Ausén B, Debnath ML, Barletta J, Price JC, Sandell J, Lopresti BJ, Wall A, Koivisto P, Antoni G, Mathis CA, Långström B: Imaging brain amyloid in Alzheimer's disease with Pittsburgh Compound-B. Ann Neurol 2004;55:306–319.
10 Kudo Y, Okamura N, Furumoto S, Tashiro M, Furukawa K, Maruyama M, Itoh M, Iwata R, Yanai K, Arai H: 2-(2-[2-dimethylaminothiazol-5-yl]ethenyl)-6-(2-[fluoro]ethoxy)benzoxazole: a novel PET agent for in vivo detection of dense amyloid plaques in Alzheimer's disease patients. J Nucl Med 2007;48:553–561.
11 Furukawa K, Okamura N, Tashiro M, Waragai M, Furumoto S, Iwata R, Yanai K, Kudo Y, Arai H: Amyloid PET in mild cognitive impairment and Alzheimer's disease with BF-227: comparison to FDG-PET. J Neurol 2010;257:721–727.
12 Verhoeff NP, Wilson AA, Takeshita S, Trop L, Hussey D, Singh K, Kung HF, Kung MP, Houle S: In vivo imaging of Alzheimer disease β-amyloid with [^{11}C]SB-13 PET. Am J Geriatr Psychiatry 2004;12:584–595.
13 Okamura N, Suemoto T, Shimadzu H, Suzuki M, Shiomitsu T, Akatsu H, Yamamoto T, Staufenbiel M, Yanai K, Arai H, Sasaki H, Kudo Y, Sawada T: Styrylbenzoxazole derivatives for in vivo imaging of amyloid plaques in the brain. J Neurosci 2004;24: 2535–2541.
14 Okamura N, Furumoto S, Funaki Y, Suemoto T, Kato M, Ishikawa Y, Ito S, Akatsu H, Yamamoto T, Sawada T, Arai H, Kudo Y, Yanai K: Binding and safety profile of novel benzoxazole derivative for in vivo imaging of amyloid deposits in Alzheimer's disease. Geriatr Gerontol Int 2007;7:393–400.
15 Waragai M, Okamura N, Furukawa K, Tashiro M, Furumoto S, Funaki Y, Kato M, Iwata R, Yanai K, Kudo Y, Arai H: Comparison study of amyloid PET and voxel-based morphometry analysis in mild cognitive impairment and Alzheimer's disease. J Neurol Sci 2009;285:100–108.
16 McKhann G, Drachman D, Folstein M, Katzman R, Price D, Stadlan EM: Clinical diagnosis of Alzheimer's disease: report of the NINCDS-ADRDA Work Group under the auspices of Department of Health and Human Services Task Force on Alzheimer's Disease. Neurology 1984;34:939–944.
17 Friston KJ, Holmes AP, Worsley KJ, Poline JP, Frith CD, Frackowiack RSJ: Statistical parametric maps in functional imaging: a general linear approach. Hum Brain Mapp 1995;2:189–210.
18 Matsuda H, Mizumura S, Nagao T, Ota T, Iizuka T, Nemoto K, Takemura N, Arai H, Homma A: Automated discrimination between very early Alzheimer disease and controls using an easy Z-score imaging system for multicenter brain perfusion single-photon emission tomography. AJNR Am J Neuroradiol 2007;28:731–736.
19 Okello A, Koivunen J, Edison P, Archer HA, Turkheimer FE, Någren K, Bullock R, Walker Z, Kennedy A, Fox NC, Rossor MN, Rinne JO, Brooks DJ: Conversion of amyloid positive and negative MCI to AD over 3 years: an ^{11}C-PiB PET study. Neurology 2009;73:754–760.
20 Arnold SE, Hyman BT, Flory J, Damasio AR, van Hoesen GW: The topographical and neuroanatomical distribution of neurofibrillary tangles and neuritic plaques in the cerebral cortex of patients with Alzheimer's disease. Cereb Cortex 1991;1:103–116.
21 Wegiel J, Bobinski M, Tarnawski M, Dziewiatkowski J, Popovitch E, Bobinski M, Lach B, Reisberg B, Miller D, de Santi S, de Leon MJ: Shift from fibrillar to nonfibrillar Aβ deposits in the neocortex of subjects with Alzheimer disease. J Alzheimers Dis 2001;3:49–57.
22 Braak H, Braak E: Neuropathological staging of Alzheimer-related changes. Acta Neuropathol 1991;82:239–259.
23 Dickson DW: The pathogenesis of senile plaques. J Neuropathol Exp Neurol 1997;56: 321–339.
24 Yamaguchi H, Nakazato Y, Shoji M, Takatama M, Hirai S: Ultrastructure of diffuse plaques in senile dementia of the Alzheimer type: comparison with primitive plaques. Acta Neuropathol 1991;82:13–20.
25 Cupidi C, Capobianco R, Goffredo D, Marcon G, Ghetti B, Bugiani O, Tagliavini F, Giaccone G: Neocortical variation of Aβ load in fully expressed, pure Alzheimer's disease. J Alzheimers Dis 2010;19:57–68.
26 Nelson PT, Abner EL, Scheff SW, Schmitt FA, Kryscio RJ, Jicha GA, Smith CD, Patel E, Markesbery WR: Alzheimer's-type neuropathology in the precuneus is not increased relative to other areas of neocortex across a range of cognitive impairment. Neurosci Lett 2009;450:336–339.

doi:10.1093/brain/awq091 Brain 2010: 133; 1772–1778 | 1772

BRAIN
A JOURNAL OF NEUROLOGY

In vivo visualization of α-synuclein deposition by carbon-11-labelled 2-[2-(2-dimethylaminothiazol-5-yl)ethenyl]-6-[2-(fluoro)ethoxy]benzoxazole positron emission tomography in multiple system atrophy

Akio Kikuchi,[1] Atsushi Takeda,[1] Nobuyuki Okamura,[2] Manabu Tashiro,[3] Takafumi Hasegawa,[1] Shozo Furumoto,[2,4] Michiko Kobayashi,[1] Naoto Sugeno,[1] Toru Baba,[1] Yasuo Miki,[5] Fumiaki Mori,[5] Koichi Wakabayashi,[5] Yoshihito Funaki,[4] Ren Iwata,[4] Shoki Takahashi,[6] Hiroshi Fukuda,[7] Hiroyuki Arai,[8] Yukitsuka Kudo,[9] Kazuhiko Yanai[2] and Yasuto Itoyama[1]

1 Department of Neurology, Graduate School of Medicine, Tohoku University, Sendai, 980-8574 Japan
2 Department of Pharmacology, Graduate School of Medicine, Tohoku University, Sendai, 980-8575 Japan
3 Division of Cyclotron Nuclear Medicine, Cyclotron and Radioisotope Centre, Tohoku University, Sendai, 980-8578 Japan
4 Division of Radiopharmaceutical Chemistry, Cyclotron and Radioisotope Centre, Tohoku University, Sendai, 980-8578 Japan
5 Department of Neuropathology, Institute of Brain Science, Hirosaki University Graduate School of Medicine, Hirosaki, 036-8562 Japan
6 Department of Diagnostic Radiology, Graduate School of Medicine, Tohoku University, Sendai, 980-8575 Japan
7 Department of Nuclear Medicine and Radiology, Institute of Development, Ageing and Cancer, Tohoku University, Sendai, 980-8575 Japan
8 Department of Geriatric and Respiratory Medicine, Institute of Development, Ageing and Cancer, Tohoku University, Sendai, 980-8575 Japan
9 Innovation of New Biomedical Engineering Centre, Tohoku University, Sendai, 980-8574 Japan

Correspondence to: Atsushi Takeda,
Department of Neurology,
Graduate School of Medicine,
Tohoku University,
1-1 Seiryo-machi,
Aoba-ku, Sendai, Miyagi,
980-8574, Japan
E-mail: atakeda@em.neurol.med.tohoku.ac.jp

The histopathological hallmark of multiple system atrophy is the appearance of intracellular inclusion bodies, named glial cytoplasmic inclusions, which are mainly composed of α-synuclein fibrils. *In vivo* visualization of α-synuclein deposition should be used for the diagnosis and assessment of therapy and severity of pathological progression in multiple system atrophy. Because 2-[2-(2-dimethylaminothiazol-5-yl)ethenyl]-6-[2-(fluoro)ethoxy] benzoxazole could stain α-synuclein-containing glial cytoplasmic inclusions in post-mortem brains, we compared the carbon-11-labelled 2-[2-(2-dimethylaminothiazol-5-yl)ethenyl]-6-[2-(fluoro)ethoxy] benzoxazole positron emission tomography findings of eight multiple system atrophy cases to those of age-matched normal controls. The positron emission tomography data demonstrated high distribution volumes in the subcortical white matter (uncorrected $P<0.001$), putamen and posterior cingulate cortex (uncorrected $P<0.005$), globus pallidus, primary motor cortex and anterior cingulate cortex (uncorrected $P<0.01$), and substantia nigra (uncorrected $P<0.05$) in multiple system atrophy cases compared to the normal controls. They were coincident with glial cytoplasmic inclusion-rich brain areas in

Received January 13, 2010. Revised March 15, 2010. Accepted March 17, 2010. Advance Access publication April 29, 2010

multiple system atrophy and thus, carbon-11-labelled 2-[2-(2-dimethylaminothiazol-5-yl)ethenyl]-6-[2-(fluoro)ethoxy] benzoxazole positron emission tomography is a promising surrogate marker for monitoring intracellular α-synuclein deposition in living brains.

Keywords: glial cytoplasmic inclusion; Lewy body; β-amyloid; Parkinson's disease; Pittsburgh compound B

Abbreviations: BF-227 = 2-[2-(2-dimethylaminothiazol-5-yl)ethenyl]-6-[2-(fluoro)ethoxy]benzoxazole; MSA = multiple system atrophy; PIB = Pittsburgh compound B

Introduction

Multiple system atrophy (MSA) is a sporadic, progressive neurodegenerative disease characterized by variable severity of parkinsonism, cerebellar ataxia, autonomic failure and pyramidal signs. Although MSA was originally described as three separate diseases [olivopontocerebellar atrophy (Dejerine and Thomas, 1900), striatonigral degeneration (van der Eecken *et al.*, 1960) and Shy–Drager syndrome (Shy and Drager, 1960)], they are currently classified into a single disease that consists of MSA with predominant parkinsonism and MSA with predominant cerebellar ataxia (Gilman *et al.*, 1999). The histopathological hallmark of MSA, glial cytoplasmic inclusions, comprises mainly insoluble fibrils of phosphorylated α-synuclein (Wakabayashi *et al.*, 1998). Thus, it is suggested that the MSA is in the family of α-synucleinopathies (Marti *et al.*, 2003) including Parkinson's disease and dementia with Lewy bodies, which are characterized by the presence of Lewy bodies, representing other brain inclusions composed of α-synuclein.

Previous neuropathological studies indicated that the appearance of glial cytoplasmic inclusions preceded the clinical onset of MSA (Fujishiro *et al.*, 2008) and the amount of α-synuclein deposition correlated with the disease progression (Wakabayashi and Takahashi, 2006). Therefore, it is plausible that the formation of α-synuclein deposits plays a key role in neurodegeneration, and that compounds that inhibit this process may be therapeutically useful for MSA and other α-synucleinopathies. In fact some compounds, including antioxidants (Ono and Yamada, 2006) and non-steroidal anti-inflammatory drugs (Hirohata *et al.*, 2008), were reported to have potent anti-fibrillogenic and fibril-destabilizing effects on aggregated α-synucleins, and received much attention as possible new therapeutic agents (Ono and Yamada, 2006; Hirohata *et al.*, 2008). Detection of α-synuclein deposition *in vivo* could theoretically allow early diagnosis even at the presymptomatic stage, as well as assess disease progression and possible therapeutic effects in the living brain of patients with MSA.

Although Pittsburgh compound B (PIB) and other compounds were reported to be useful in detecting senile plaques *in vivo*, to our knowledge, there were no imaging probes currently available for *in vivo* detection of α-synuclein deposition. Recently, 2-[2-(2-dimethylaminothiazol-5-yl)ethenyl]-6-[2-(fluoro)ethoxy] benzoxazole (BF-227), known as a positron emission tomography (PET) probe for *in vivo* detection of dense β-amyloid deposits in humans (Kudo *et al.*, 2007), was reported to bind with synthetic α-synuclein aggregates as well as β-amyloid fibrils *in vitro* (Fodero-Tavoletti *et al.*, 2009). In the present study, we demonstrated that BF-227 could stain α-synuclein-containing glial cytoplasmic inclusions in post-mortem tissues and moreover, that a PET study with carbon-11-labelled BF-227 ([11C]-BF-227) could detect α-synuclein deposits in the living brains of patients with MSA.

Materials and methods

Neuropathological staining

Brain specimens

The subjects of the first part of the study were nine autopsy cases, including three with Parkinson's disease, three with dementia with Lewy bodies and three with MSA. The above diagnoses were confirmed both clinically and histopathologically. Brain tissues taken from the temporal cortex and substantia nigra of patients with Parkinson's disease and dementia with Lewy bodies, and pontine base of patients with MSA, were fixed in 20% buffered formalin for 72 h at 4°C, and vibratome sections (50 μm thick) were prepared.

Fluorescence and immunohistochemical analysis

BF-227 was dissolved in 50% ethanol containing 5% polysorbate (Tween 80; Wako, Osaka, Japan). The sections were slide mounted, incubated in 100 μM BF-227 for 30 min, dipped three times in phosphate buffer, and coverslipped with non-fluorescent mounting medium (Vectashield, Vector Laboratories, Burlingame, CA, USA). Fluorescence images were visualized using an Olympus Provis fluorescence microscope (Olympus, Tokyo, Japan) at wavelength 400 nm. After photographing fluorescent structures, BF-227-labelled sections were immunostained with primary antibodies against phosphorylated α-synuclein (#64; Wako). For phosphorylated α-synuclein immunohistochemistry, the sections were pre-treated with 99% formic acid for 5 min, then incubated overnight at 4°C with each primary antibody followed by incubation with the biotinylated secondary antibodies and the avidin–biotin–peroxidase complex (Vectastain ABC kit, Vector Laboratories). Diaminobenzidine was used as the chromogen.

PET study

Subjects

Eight patients with probable MSA and eight age-matched normal subjects were studied to examine the distribution of [11C]-BF-227 in the brain. All probable MSA patients were diagnosed on the second consensus criteria for probable MSA (Gilman *et al.*, 2008). Table 1 summarizes the clinical features of these patients. There were no significant differences in age, disease duration and unified MSA rating scale score between the MSA with predominant parkinsonism

Table 1 Subject profile

	Normal controls	MSA		
		Total	MSA-P	MSA-C
n	8	8	4	4
Gender (F/M)	4/4	4/4	1/3	3/1
Age (years)	64.3 ± 5.90	57.4 ± 10.1	60.5 ± 11.1	54.3 ± 9.50
Duration (years)		1.50 ± 0.54	1.75 ± 0.50	1.25 ± 0.50
UMSARS score		36.1 ± 8.87	41.5 ± 9.39	30.8 ± 4.27

Data are mean ± SD.
MSA-P = MSA with predominant parkinsonism; MSA-C = MSA with predominant cerebellar ataxia; UMSARS = unified MSA rating scale.

subgroup and the MSA with predominant cerebellar ataxia subgroup. The normal control group comprised volunteers without impairment of cognitive and motor functions who had no cerebrovascular lesions on magnetic resonance imaging. The study protocol was approved by the Ethical Committee of Tohoku University Graduate School of Medicine, and a written informed consent was obtained from each subject after being given a complete description of the study.

Radiosynthesis of [^{11}C]-BF-227

BF-227 and its N-desmethylated derivative (a precursor of [^{11}C]-BF-227) were custom-synthesized by Tanabe R&D Service Co. (Tokyo) (Kudo *et al.*, 2007). [^{11}C]-BF-227 was synthesized from the precursor by N-methylation in dimethyl sulphoxide using [^{11}C]-methyl triflate (Jewett, 1992; Iwata *et al.*, 2001). After quenching the reaction with 5% acetic acid in ethanol, [^{11}C]-BF-227 was separated from the crude mixture by semi-preparative reversed-phase high-performance liquid chromatography and then isolated from the collected fraction by solid-phase extraction. The purified [^{11}C]-BF-227 was solubilized in isotonic saline containing 1% polysobate-80 and 5% ascorbic acid. The saline solution was filter sterilized with a 0.22 mm Millipore® filter for clinical use. The radiochemical yields were >50% based on [^{11}C]-methyl triflate, and the specific radioactivities were 119–138 GBq/mmol at the end of synthesis. The radiochemical purities were >95%.

PET procedure

The [^{11}C]-BF-227 PET study was performed using a SET-2400W PET scanner (Shimadzu Inc., Japan) under resting condition with eyes closed in a dark room. Following a 68Ge/Ga transmission scan of 300–400 s duration, an emission scan was started soon after intravenous injection of 3.7–8.3 mCi of [^{11}C]-BF-227. A dynamic series of PET scans were acquired over 60 min with 23 frames. Emission data were corrected for attenuation, dead time and radioactive decay. Standardized uptake value images were obtained by normalizing tissue concentration by the injected dose and body mass. Arterial blood samples (1.5 ml) from the radial or brachial artery were collected from each subject at 10 s intervals for the first 2 min, and subsequently at intervals increasing progressively from 1 to 10 min until 60 min after the injection of [^{11}C]-BF-227 except for one subject, from whom arterialized venous blood samples (1.5 ml) from a hand vein heated in a far-infrared mat were collected at the same time intervals. The plasma obtained by centrifugation at 3000*g* for 3 min was weighed and the radioactivity was measured with a well-type scintillation counter. Additional arterial blood samples were obtained at four time points during the study (5, 15, 30 and 60 min) for the determination of radiolabelled metabolites in plasma using high-performance liquid chromatography. These data yielded values of the unchanged fraction of parent radiotracer throughout the time frame of the study. A multi-exponential equation was used to describe this curve and to estimate the parent fraction at each measured plasma curve time point.

PET image analysis

To measure α-synuclein deposition densities in the brain, the distribution volume, the ratio of [^{11}C]-BF-227 concentration in tissue to that in plasma at equilibrium, was calculated by Logan's graphical analysis (Logan, 2000), since BF-227 reversibly binds to α-synuclein depositions (Tashiro *et al.*, 2009). Region of interest analysis was performed to evaluate the regional distribution of [^{11}C]-BF-227. Circular regions of interest were placed on individual axial PET images in the frontal cortex, primary motor cortex, parietal cortex, medial temporal cortex, lateral temporal cortex, occipital cortex, anterior cingulate cortex, posterior cingulate cortex, subcortical white matter, caudate nucleus, putamen, globus pallidus, thalamus, substantia nigra, midbrain tegmentum, pons and cerebellar cortex, referring to the individual magnetic resonance images.

Statistical analysis

Data were expressed as mean ± SD. Differences in distribution volume between normal control and MSA groups were evaluated by one-way analysis of variance followed by Bonferroni's multiple comparison test (GraphPad Prism Software).

Results

Neuropathological staining

In the post-mortem brains with Parkinson's disease, double-labelling immunostaining with BF-227 fluorostaining and anti-phosphorylated α-synuclein antibody demonstrated co-localization of the proteins in Lewy bodies in the substantia nigra (Fig. 1A and B). Strong BF-227 staining was observed in the central core (Fig. 1A). BF-227 was also detected in the cortical Lewy bodies in dementia with Lewy bodies (Fig. 1C and D). In MSA, double-labelling experiments using BF-227 and anti-phosphorylated α-synuclein antibody demonstrated BF-227 fluorescent signal in the most of glial cytoplasmic inclusions in the pontine base (Fig. 1E and F).

PET study

Tissue time activity curves of [^{11}C]-BF-227 in the brain indicated more gradual clearance from the brain in patients with MSA compared with normal subjects following initial rapid uptake of radioactivity (Fig. 2A). Relatively high concentrations of [^{11}C]-BF-227 radioactivity were observed in the subcortical white matter and lenticular nucleus in MSA, in which relatively intense α-synuclein deposits were found in the post-mortem brain (Fig. 2B). [^{11}C]-BF-227 exhibited linear regression curves on Logan plot analysis in all brain regions examined. Since the slopes of the regression lines represent the distribution volume of the tracer, these findings indicated a higher distribution volume of [^{11}C]-BF-227 in MSA than in normal controls (Fig. 2C). The regional distribution volume values were high in the subcortical white matter (uncorrected $P<0.001$), putamen and posterior cingulate cortex

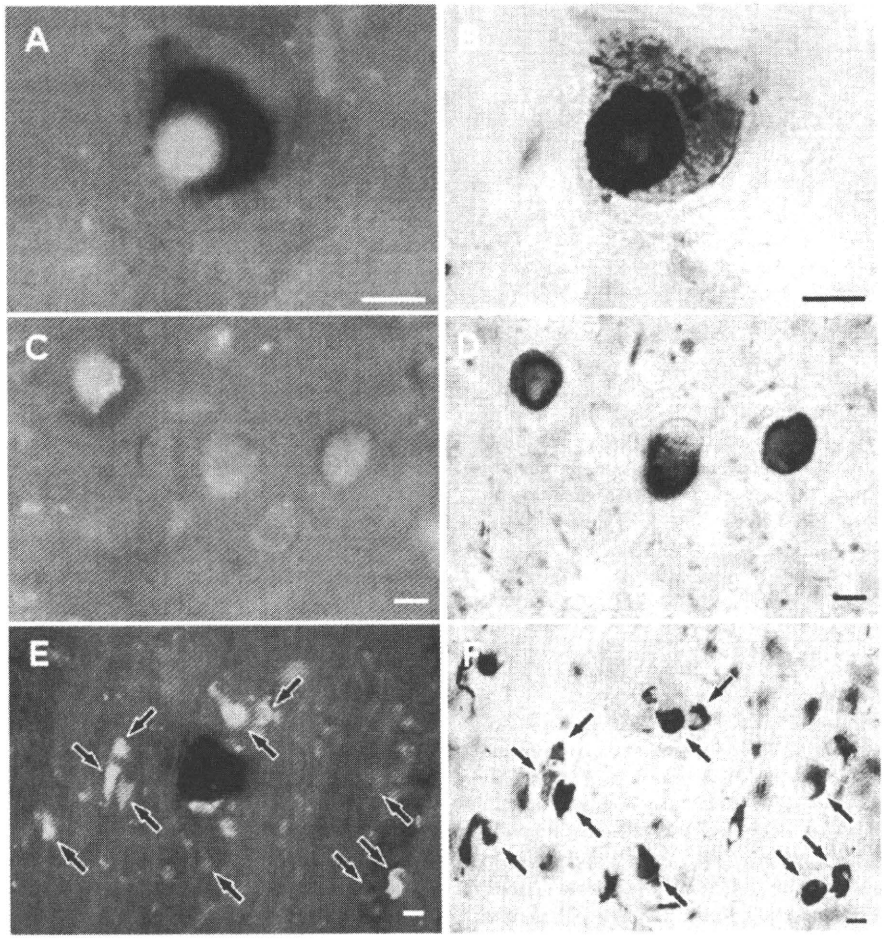

Figure 1 Neuropathological findings of BF-227 fluorostaining and anti-phosphorylated α-synuclein antibody immunostaining. BF-227 fluorostaining (**A** and **C**) and anti-phosphorylated α-synuclein antibody immunostaining (**B** and **D**) showed colocalization of these proteins in brainstem-type Lewy bodies in the substantia nigra of patients with Parkinson's disease (**A** and **B**) and in cortical Lewy bodies in the temporal lobe of patients dementia with Lewy bodies (**C** and **D**). Similarly, BF-227 fluorostaining (**E**) and anti-phosphorylated α-synuclein antibody immunostaining (**F**) were codetected in glial cytoplasmic inclusions in the pontine base of a patient with MSA. BF-227 histofluorescence was observed in the most of glial cytoplasmic inclusions (arrows). Bars = 10 μm.

(uncorrected $P<0.005$), globus pallidus, primary motor cortex and anterior cingulate cortex (uncorrected $P<0.01$) and substantia nigra (uncorrected $P<0.05$) in patients with MSA compared to the normal controls (Table 2 and Fig. 2D). It is noteworthy that the distribution volume of [^{11}C]-BF-227 was significantly high in the subcortical white matter even if Bonferroni's multiple comparison test was applied. On the other hand, no obvious differences were found in either the distribution or degree of binding between the MSA with predominant parkinsonism and MSA with predominant cerebellar ataxia subgroups.

Discussion

The BF-227 stained α-synuclein-containing Lewy bodies (Fig. 1A–D) and glial cytoplasmic inclusions (Fig. 1E and F) in formalin-fixed tissue sections as well as β-amyloid-containing senile plaques in paraffin-embedded tissue sections (Kudo *et al.*, 2007). These results were consistent with the previous findings showing BF-227 binding to synthetic α-synuclein fibrils with high affinity (K_d 9.63 nM) (Fodero-Tavoletti *et al.*, 2009), and to Lewy bodies in paraffin-embedded tissue sections (Fodero-Tavoletti *et al.*, 2009).

The anti-phosphorylated α-synuclein antibody immunostained the halo region more intensively compared with the central core in Lewy bodies in the substantia nigra of Parkinson's disease, while the BF-227 staining was intensely observed in the core of Lewy bodies (Fig. 1A and B). Because intense thioflavin S staining was also reported in the core of nigral Lewy bodies (Duda *et al.*, 2000), the core is thought to be rich in β-sheet structures. Similar to thioflavin S, the BF-227 staining is considered to recognize amyloid-like β-pleated sheets, and it was suggested to be the reason for the more intense BF-227 staining in the core of Lewy bodies. In addition, the high density of the core structure

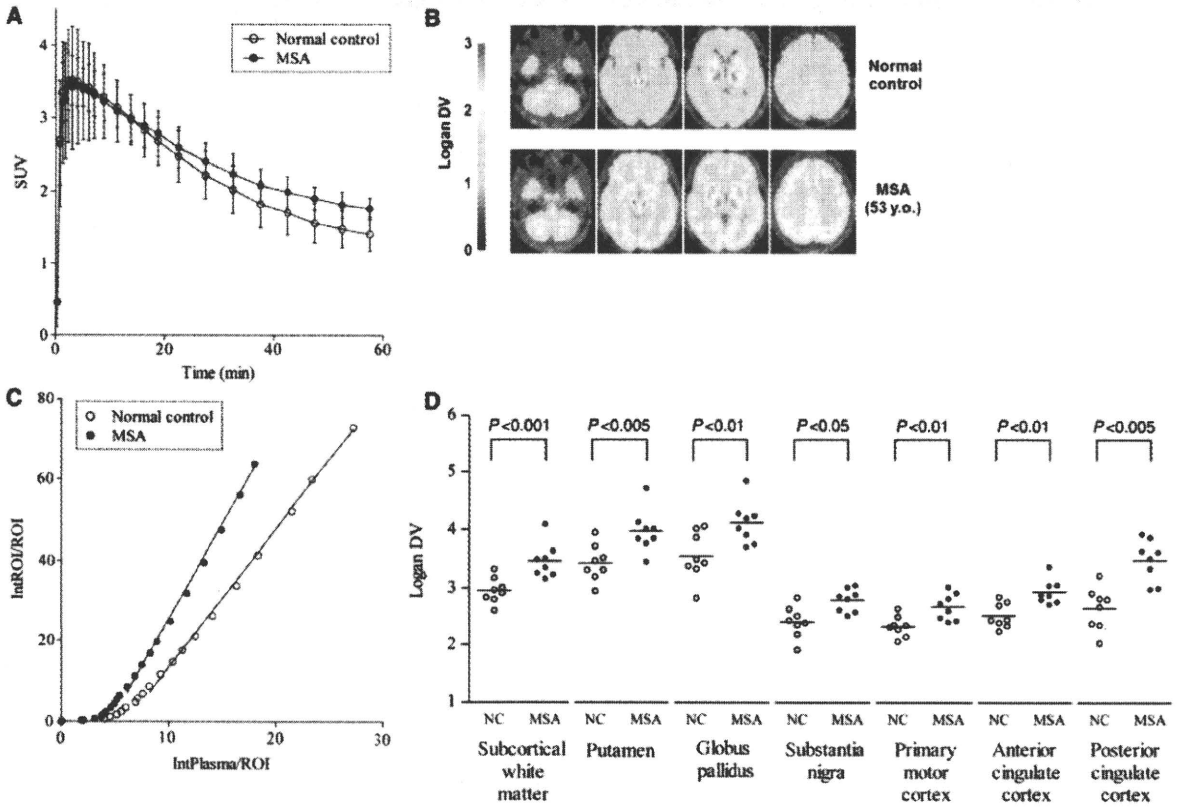

Figure 2 [^{11}C]-BF-227 PET findings in MSA. Time activity curves showed initial rapid uptake of radioactivity followed by gradual clearance in the putamen of both normal subjects and MSA cases. Data are mean ± SD of eight normal subjects and eight patients with MSA (**A**). In a representative patient with MSA with predominant cerebellar ataxia, the regional distribution volumes were mapped to the subcortical white matter and lentiform nucleus compared to normal control (**B**). Typical Logan plots for the putamen were presented in a representative patient with MSA with predominant cerebellar ataxia and a normal control. The slopes of the linear regression curves on Logan plot analysis represent the distribution volume of the tracer in the putamen (**C**). There were differences in the mean regional distribution volume values between patients with MSA and normal control in the subcortical white matter (uncorrected $P<0.001$), putamen and posterior cingulate cortex (uncorrected $P<0.005$), globus pallidus, primary motor cortex and anterior cingulate cortex (uncorrected $P<0.01$) and substantia nigra (uncorrected $P<0.05$). Data of individual subjects (symbols) and mean values (horizontal lines) (**D**). SUV = standardized uptake value; DV = distribution volume; ROI = region of interest.

may often prevent the penetration of antibodies into this region (Galloway *et al.*, 1992), since electron microscopic studies revealed that vesicular structures were tightly packed in the core of Lewy bodies (Takahashi and Wakabayashi, 2005). On the other hand, not all glial cytoplasmic inclusions stained by anti-phosphorylated α-synuclein antibody were always positive for BF-227 staining (Fig. 1E and F). In the process of oligodendroglial pathology, it was believed that α-synuclein deposits as amorphous state and then forms fibrillar structures (Gai *et al.*, 2003; Stefanova *et al.*, 2005). In fact, part of glial cytoplasmic inclusions were reported to be α-synuclein-negative (Sakamoto *et al.*, 2005) and therefore, it seems reasonable that some of glial cytoplasmic inclusions were not composed of β-sheet fibrils and were negative for BF-227 staining.

The regional distribution volume of [^{11}C]-BF-227 was the highest in the subcortical white matter, followed by the putamen, posterior cingulate cortex, anterior cingulate cortex, globus pallidus, primary motor cortex and substantia nigra, in which glial cytoplasmic inclusions were densely distributed (Papp and Lantos, 1994; Inoue *et al.*, 1997; Wakabayashi and Takahashi, 2006) and large increases of α-synuclein content were found (Tong *et al.*, 2010) in the post-mortem brains. Thus, it was suggested that the distributions of [^{11}C]-BF-227 could properly reflect those of the α-synuclein deposits *in vivo*. On the other hand, the regional distribution volume in other affected brain regions, such as the cerebellum and pons (Ozawa *et al.*, 2004; Wakabayashi and Takahashi, 2006), did not show higher values relative to the normal control group. The glial cytoplasmic inclusions in cerebellum were reported to decrease along with the disease progression and concomitant neuronal loss (Inoue *et al.*, 1997). Therefore, it is plausible that the accumulation levels of glial cytoplasmic inclusions are changing and do not always increase with the disease progression (Mochizuki *et al.*, 1992; Inoue *et al.*, 1997). Moreover, due to the remarkable cerebellar and pontine atrophy,

Table 2 Distribution volume of [^{11}C]BF-227

	Normal controls	MSA
Frontal cortex	2.28 ± 0.18	2.46 ± 0.22
Primary motor cortex	2.40 ± 0.28	2.79 ± 0.20¶
Parietal cortex	2.48 ± 0.26	2.63 ± 0.24
Medial temporal cortex	2.44 ± 0.21	2.82 ± 0.31
Lateral temporal cortex	2.42 ± 0.19	2.63 ± 0.23
Occipital cortex	2.43 ± 0.20	2.72 ± 0.27
Anterior cingulate cortex	2.32 ± 0.18	2.67 ± 0.23¶
Posterior cingulate cortex	2.52 ± 0.22	2.94 ± 0.22†
Subcortical white matter	2.65 ± 0.38	3.49 ± 0.36‡
Caudate nucleus	2.70 ± 0.21	3.05 ± 0.34
Putamen	2.95 ± 0.23	3.47 ± 0.30†
Globus pallidus	3.43 ± 0.31	3.97 ± 0.36¶
Thalamus	3.50 ± 0.28	4.03 ± 0.31
Substantia nigra	3.55 ± 0.41	4.12 ± 0.36*
Midbrain tegmentum	3.53 ± 0.54	3.45 ± 0.47
Pons	3.63 ± 0.54	3.88 ± 0.42
Cerebellar cortex	2.32 ± 0.22	2.16 ± 0.29

Data are mean ± SD.
*Uncorrected $P < 0.05$.
¶Uncorrected $P < 0.01$.
†Uncorrected $P < 0.005$.
‡Uncorrected $P < 0.001$.

the distribution volume in these regions might be underestimated. Correction for partial volume loss is therefore needed to improve the accuracy of quantification in the cerebellum and brainstem of MSA. BF-227 fluorescent signal was detected in β-amyloid plaques as well as glial cytoplasmic inclusions and Lewy bodies (Fig. 1A–F) in neuropathological staining (Kudo *et al.*, 2007). However, the differences in the distribution of [^{11}C]-BF-227 by PET could discriminate MSA from Alzheimer's disease, which showed high distribution of [^{11}C]-BF-227 in the temporoparietal–occipital region (Kudo *et al.*, 2007). In our preliminary studies, Parkinson's disease and dementia with Lewy bodies also showed quite different patterns of distribution volumes from those of MSA (data not shown). Therefore, MSA could be distinguished from other degenerative diseases such as Alzheimer's disease, Parkinson's disease and dementia with Lewy bodies by the [^{11}C]-BF-227 PET.

The affinity of BF-227 to α-synuclein fibrils (K_d 9.63 nM) was reported to be almost identical to that of PIB (K_d 10.07 nM) (Fodero-Tavoletti *et al.*, 2007, 2009). However, in the post-mortem human brain, the PIB binding was not colocalized with α-synuclein-positive Lewy bodies in two reports (Fodero-Tavoletti *et al.*, 2007; Ye *et al.*, 2008) although one report showed PIB binding to Lewy bodies in the substantia nigra of Parkinson's disease (Maetzler *et al.*, 2008). Therefore, there is controversy as to whether PIB binds to α-synuclein-containing Lewy bodies. Moreover, there have been no reports showing that PIB could detect α-synuclein deposits in α-synucleinopathies by PET (Fodero-Tavoletti *et al.*, 2007; Johansson *et al.*, 2008; Maetzler *et al.*, 2008). The hydroxy group in PIB (Mathis *et al.*, 2003) may prevent it from passing through the cell membranes and thereby detecting α-synuclein depositions in the cytoplasm, however, the BF-227 is more lipophilic than PIB (Mathis *et al.*, 2003), and may easily pass into the cytoplasm and bind to α-synuclein aggregates. As shown in the present study, BF-227 is a promising tracer to detect glial cytoplasmic inclusions. Further studies are warranted to verify whether Lewy bodies in other α-synucleinopathies as well as glial cytoplasmic inclusions can be detected by [^{11}C]-BF-227 PET.

In conclusion, the BF-227 could bind to α-synuclein-containing glial cytoplasmic inclusions (Fig. 1E and F) in the post-mortem brain, and the [^{11}C]-BF-227 PET demonstrated high signals in the glial cytoplasmic inclusion-rich brain regions including subcortical white matter, putamen, globus pallidus, primary motor cortex and anterior and posterior cingulate cortex (Table 2 and Fig. 2D). These results suggest that [^{11}C]-BF-227 PET is a suitable surrogate maker for monitoring α-synuclein deposits in living brains with MSA and could be a potential tool to monitor the effectiveness of neuroprotective therapy for α-synucleinopathies.

Funding

Grant for 'the Research Committee for Ataxic Diseases' of the Research on Measures for Intractable Diseases from the Ministry of Health, Labour and Welfare, Japan (partial).

References

Dejerine J, Thomas A. L'atrophie olivo-ponto-cérébelleuse. Nouvelle Iconographie Salpêtrière 1900; 13: 330–7.

Duda JE, Lee VM, Trojanowski JQ. Neuropathology of synuclein aggregates. J Neurosci Res 2000; 61: 121–7.

Fodero-Tavoletti MT, Mulligan RS, Okamura N, Furumoto S, Rowe CC, Kudo Y, et al. In vitro characterisation of BF227 binding to alpha-synuclein/Lewy bodies. Eur J Pharmacol 2009; 617: 54–8.

Fodero-Tavoletti MT, Smith DP, McLean CA, Adlard PA, Barnham KJ, Foster LE, et al. In vitro characterization of Pittsburgh compound-B binding to Lewy bodies. J Neurosci 2007; 27: 10365–71.

Fujishiro H, Ahn TB, Frigerio R, DelleDonne A, Josephs KA, Parisi JE, et al. Glial cytoplasmic inclusions in neurologically normal elderly: prodromal multiple system atrophy? Acta Neuropathol 2008; 116: 269–75.

Gai WP, Pountney DL, Power JH, Li QX, Culvenor JG, McLean CA, et al. alpha-Synuclein fibrils constitute the central core of oligodendroglial inclusion filaments in multiple system atrophy. Exp Neurol 2003; 181: 68–78.

Galloway PG, Mulvihill P, Perry G. Filaments of Lewy bodies contain insoluble cytoskeletal elements. Am J Pathol 1992; 140: 809–22.

Gilman S, Low PA, Quinn N, Albanese A, Ben-Shlomo Y, Fowler CJ, et al. Consensus statement on the diagnosis of multiple system atrophy. J Neurol Sci 1999; 163: 94–8.

Gilman S, Wenning GK, Low PA, Brooks DJ, Mathias CJ, Trojanowski JQ, et al. Second consensus statement on the diagnosis of multiple system atrophy. Neurology 2008; 71: 670–6.

Hirohata M, Ono K, Morinaga A, Yamada M. Non-steroidal anti-inflammatory drugs have potent anti-fibrillogenic and fibril-destabilizing effects for alpha-synuclein fibrils in vitro. Neuropharmacology 2008; 54: 620–7.

Inoue M, Yagishita S, Ryo M, Hasegawa K, Amano N, Matsushita M. The distribution and dynamic density of oligodendroglial cytoplasmic inclusions (GCIs) in multiple system atrophy: a correlation between the density of GCIs and the degree of involvement of striatonigral and olivopontocerebellar systems. Acta Neuropathol 1997; 93: 585–91.

Iwata R, Pascali C, Bogni A, Miyake Y, Yanai K, Ido T. A simple loop method for the automated preparation of (11C)raclopride from (11C)methyl triflate. Appl Radiat Isot 2001; 55: 17–22.

Jewett DM. A simple synthesis of [11C]methyl triflate. Int J Rad Appl Instrum [A] 1992; 43: 1383–5.

Johansson A, Savitcheva I, Forsberg A, Engler H, Langstrom B, Nordberg A, et al. [(11)C]-PIB imaging in patients with Parkinson's disease: preliminary results. Parkinsonism Relat Disord 2008; 14: 345–7.

Kudo Y, Okamura N, Furumoto S, Tashiro M, Furukawa K, Maruyama M, et al. 2-(2-[2-Dimethylaminothiazol-5-yl]ethenyl)-6-(2-[fluoro]ethoxy)benzoxazole: a novel PET agent for in vivo detection of dense amyloid plaques in Alzheimer's disease patients. J Nucl Med 2007; 48: 553–61.

Logan J. Graphical analysis of PET data applied to reversible and irreversible tracers. Nucl Med Biol 2000; 27: 661–70.

Maetzler W, Reimold M, Liepelt I, Solbach C, Leyhe T, Schweitzer K, et al. [11C]PIB binding in Parkinson's disease dementia. Neuroimage 2008; 39: 1027–33.

Marti MJ, Tolosa E, Campdelacreu J. Clinical overview of the synucleinopathies. Mov Disord 2003; 18(Suppl): S21–7.

Mathis CA, Wang Y, Holt DP, Huang GF, Debnath ML, Klunk WE. Synthesis and evaluation of 11C-labeled 6-substituted 2-arylbenzothiazoles as amyloid imaging agents. J Med Chem 2003; 46: 2740–54.

Mochizuki A, Mizusawa H, Ohkoshi N, Yoshizawa K, Komatsuzaki Y, Inoue K, et al. Argentophilic intracytoplasmic inclusions in multiple system atrophy. J Neurol 1992; 239: 311–6.

Ono K, Yamada M. Antioxidant compounds have potent anti-fibrillogenic and fibril-destabilizing effects for alpha-synuclein fibrils in vitro. J Neurochem 2006; 97: 105–15.

Ozawa T, Paviour D, Quinn NP, Josephs KA, Sangha H, Kilford L, et al. The spectrum of pathological involvement of the striatonigral and olivopontocerebellar systems in multiple system atrophy: clinicopathological correlations. Brain 2004; 127: 2657–71.

Papp MI, Lantos PL. The distribution of oligodendroglial inclusions in multiple system atrophy and its relevance to clinical symptomatology. Brain 1994; 117(Pt 2): 235–43.

Sakamoto M, Uchihara T, Nakamura A, Mizutani T, Mizusawa H. Progressive accumulation of ubiquitin and disappearance of alpha-synuclein epitope in multiple system atrophy-associated glial cytoplasmic inclusions: triple fluorescence study combined with Gallyas-Braak method. Acta Neuropathol 2005; 110: 417–25.

Shy GM, Drager GA. A neurological syndrome associated with orthostatic hypotension: a clinical-pathologic study. Arch Neurol 1960; 2: 511–27.

Stefanova N, Reindl M, Neumann M, Haass C, Poewe W, Kahle PJ, et al. Oxidative stress in transgenic mice with oligodendroglial alpha-synuclein overexpression replicates the characteristic neuropathology of multiple system atrophy. Am J Pathol 2005; 166: 869–76.

Takahashi H, Wakabayashi K. Controversy: is Parkinson's disease a single disease entity? Yes. Parkinsonism Relat Disord 2005; 11(Suppl 1): S31–7.

Tashiro M, Okamura N, Furumoto S, Kumagai K, Furukawa K, Sugi K, et al. Quantitative analysis of amyloid deposition in Alzheimer's disease patients and healthy volunteers using PET and [11C]BF-227. In: Proceedings of the International Symposium on Early Detection and Rehabilitation Technology of Dementia 2009 (DRD2009). Okayama, Japan, 2009.110–1.

Tong J, Wong H, Guttman M, Ang LC, Forno LS, Shimadzu M, et al. Brain alpha-synuclein accumulation in multiple system atrophy, Parkinson's disease and progressive supranuclear palsy: a comparative investigation. Brain 2010; 133: 172–88.

van der Eecken H, Adams RD, van Bogaert L. Striopallidal-nigral degeneration. An hitherto undescribed lesion in paralysis agitans. J Neuropathol Exp Neurol 1960; 19: 159–61.

Wakabayashi K, Takahashi H. Cellular pathology in multiple system atrophy. Neuropathology 2006; 26: 338–45.

Wakabayashi K, Yoshimoto M, Tsuji S, Takahashi H. Alpha-synuclein immunoreactivity in glial cytoplasmic inclusions in multiple system atrophy. Neurosci Lett 1998; 249: 180–2.

Ye L, Velasco A, Fraser G, Beach TG, Sue L, Osredkar T, et al. In vitro high affinity alpha-synuclein binding sites for the amyloid imaging agent PIB are not matched by binding to Lewy bodies in postmortem human brain. J Neurochem 2008; 105: 1428–37.

Ann Nucl Med
DOI 10.1007/s12149-010-0381-y

ORIGINAL ARTICLE

Long-term performance evaluation of positron emission tomography: analysis and proposal of a maintenance protocol for long-term utilization

Shoichi Watanuki · Manabu Tashiro · Masayasu Miyake · Yoichi Ishikawa · Masatoshi Itoh · Kazuhiko Yanai · Yasuhiro Sakemi · Hiroshi Fukuda · Keizo Ishii

Received: 22 July 2009 / Accepted: 26 March 2010

Abstract

Objective Positron emission tomography (PET) scanners require periodic monitoring in order to maintain scanner performance. The aim of the present study was to examine the deterioration of PET scanner performance caused by aging.

Methods We retrospectively examined PET scanner performance alterations in terms of sensitivity, spatial resolution, false coincidences due to scatter and random coincidences based on 13 years of follow-up data, including data when the PET scanner underwent an overhaul at the 10th year after installation. Sensitivity and scatter fraction were calculated by using cross calibration factor (CCF) measurement data, which are collected routinely. Efficacy of the examining the sensitivity and scatter was confirmed by NEMA measurements. Trans-axial resolution was measured as full width at half-maximum (FWHM) and full width at tenth-maximum (FWTM) at 0–20 cm offset from the field of view (FOV) center at the time of installation, 8 years after installation, and immediately after the overhaul. Random coincidence rate fraction was measured in a wide range of count rates before and after the overhaul.

Results and discussion The results indicated that the total reduction of sensitivity during the first 10 years was 41% of the initial value in terms of NEMA measurement, and that the annual reduction of sensitivity progressed at a rate of 4.7% per year in terms of CCF measurement data. The changes in sensitivity can be calculated using CCF measurement data. Regarding the spatial resolution, mean FWHM and FWTM values were increased by 1.7 and 3.6%, respectively, in 8 years after installation. The relative scatter fraction was significantly increased compared with that before the overhaul. The random fraction decreased by 10–15% after the overhaul within a certain range of random count rates (1–120 kcps). In the case of our scanner, the parameter that displayed the largest change was the sensitivity, and this change was thought to be caused by the reduction of photomultiplier tube (PMT) gain, although the changes in PMT gain can cause various types of performance deterioration, as investigated in this study.

Conclusion We observed that the sensitivity of our PET scanner generally deteriorated due to aging. Sensitivity monitoring using CCF measurements can be an easy and useful method for monitoring and maintaining the performance of PET scanners against aging. Since the data were obtained from a single scanner, the authors would encourage the initiation of a follow-up study involving various scanners.

S. Watanuki · M. Tashiro (✉) · M. Miyake · M. Itoh · K. Yanai · H. Fukuda · K. Ishii
Division of Cyclotron Nuclear Medicine, Cyclotron and Radioisotope Center, Tohoku University, 6-3 Aoba, Aramaki, Aoba-ku, Sendai, Miyagi 980-8578, Japan
e-mail: mtashiro@m.tains.tohoku.ac.jp

Y. Ishikawa
Division of Radiopharmaceutical Chemistry, Cyclotron and Radioisotope Center, Tohoku University, 6-3 Aoba, Aramaki, Aoba-ku, Sendai, Miyagi 980-8578, Japan

Y. Sakemi
Division of Instrumentations, Cyclotron and Radioisotope Center, Tohoku University, 6-3 Aoba, Aramaki, Aoba-ku, Sendai, Miyagi 980-8578, Japan

H. Fukuda
Institute of Development, Aging and Cancer, Tohoku University, Aoba-ku, Sendai, Japan

K. Ishii
Department of Quantum Science and Energy Engineering, Graduate School of Engineering, Tohoku University, Aoba-ku, Sendai, Japan

Published online: 20 April 2010

Keywords Positron emission tomography (PET) · Quality control · Cross calibration

Introduction

Positron emission tomography (PET) has been widely used for the diagnosis of various illnesses, such as cancer and neurological and cardiac disorders, as well as for drug development [1–5]. Widespread use of the PET technique is attributable to its high resolution, high sensitivity, and quantification abilities, as well as the wide availability of radiopharmaceuticals for imaging in comparison to conventional nuclear medicine. Its disadvantages include the relatively high costs for installation and maintenance. For daily routine examinations using PET, consistent scanner performance is necessary in order to maintain a reliable examination quality. However, aging of the scanner is unavoidable, and its performance tends to deteriorate with age. Therefore, PET scanners require periodic performance monitoring in order to maintain their performance at a satisfactory level [6].

Several guidelines for performance evaluation have been proposed by a number of organizations, such as the International Electrotechnical Committee (IEC) [7], American College of Radiology (ACR) [8], and Japan Industries Association of Radiological Systems (JIRA) [9]. However, recommended intervals for examination range from once a week to once a year according to the different guidelines, and a unification of the different standards has not yet been achieved (Table 1). In addition, none of the organizations has provided supporting data regarding how the recommended frequency of monitoring was determined.

Precise information is important in order to determine how to monitor the deterioration in scanner performance, as well as how frequently the monitoring procedures should be performed. It is noteworthy that the current performance monitoring procedures are time- and energy-consuming. Consequently, it would be useful to know how often scanner performance should be examined based on concrete and reliable data, and it would also be helpful to formulate a simple protocol for the early detection of performance deterioration. To the best of our knowledge, although many studies have reported scanner performance at an early stage of installation [10–12] and performance deterioration during a short period of less than 1 year after installation [13, 14], little attention has been paid to the changes in the PET scanner performance due to aging over several years of use, except in a few previous studies [6, 15, 16]. We previously examined the relationship between aging and performance deterioration in one of our PET scanners [6]. This study showed that the sensitivity of the scanner (PT931/04: CTI Inc., Knoxville, USA) decreased to 72% of its initial value after 13 years, whereas resolution was kept at the initial performance level. Matsumoto et al. [15] also reported that the sensitivity of another PET scanner decreased to 92.3% of its initial value after 6 years. On the other hand, Zhang et al. [16] reported good performance stability of sensitivity and resolution in re-evaluating a system performance of an animal PET scanner after 6 years of use. Thus, the aim of our present study is to retrospectively analyze the data of PET scanner performance; the data were serially collected over 13 years after first installation. This analysis would provide not only the characteristics of performance deterioration due to aging in terms of sensitivity, spatial resolution, scatter fraction and random coincidences, but will also provide basic data to determine the optimum interval for performance evaluation.

Table 1 Recommended procedures and frequency of performance tests for PET scanners

Test item	Organization		
	IEC	ACR	JIRA
Resolution	2/year	1/year	1/month
Sensitivity	–	1/year	1/week
Relative sensitivity of the line of response[a]	Daily	–	–
Uniformity	–	1/year	1/month
Count rate performance	–	1/year	1/month
Correction accuracy	–	1/year	–
Image contrast	–	1/year	–
Pixel size	2/year	–	–
Cross-calibration	>2/year	–	–

IEC International Electrotechnical Committee, *ACR* American College of Radiology, *JIRA* Japan Industries Association of Radiological Systems

[a] The relative sensitivity of the line of response is related to the average of the overall sensitivity per line of response

Methods

System description

The follow-up data of scanner performance were obtained from our PET scanner (SET-2400W: Shimadzu Co. Ltd., Kyoto, Japan) at Tohoku University Cyclotron and Radioisotope Center. The scanner consists of four rings of 112 BGO detector blocks. Each detector block has a 6 (in-plane) × 8 (axial) matrix of BGO crystals coupled to two dual photomultiplier tubes (PMTs). The crystal size is 3.8 mm (in-plane), 6.25 mm (axial) and 30 mm (depth). These are arranged in 32 rings with 672 crystals each, giving 63 two-dimensional (2D) image planes. The scanner has an axial field of view (FOV) of 20 cm long and a

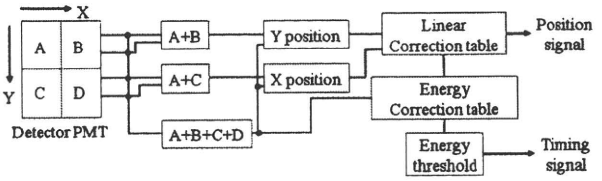

Fig. 1 Block diagram of detector signal process. Measuring the coincidences involves conversion of 4 PMT signals from detector blocks into crystal positions and timing signals by using linear and energy correction tables. These tables are adjusted for a well-balanced and constant photomultiplier tube (PMT) gain signal. Therefore, the stability of the gain and the balance of the PMTs is an important factor for the sensitivity and resolution of detector systems, as well as for maintenance of the performance

transaxial FOV of 59.5 cm diameter in 2D and 3D data acquisition. Signals from the PMTs are processed to the position of the crystal in which gamma photon hits by using a coincidence time window of 15 ns. Position non-linearity and energy non-uniformity of the detector block are corrected in real-time by using position and energy correction tables [10]. Figure 1 shows detailed information of the position detection circuit.

Determination of the cross calibration factors (CCFs) was performed once a week by using a cylinder phantom before starting the weekly clinical examinations. Periodic maintenance has been performed on the scanner every 6 months by a maintenance supplier. The maintenance procedures include adjustment of the detector system in terms of PMT gain and balance and timing of coincidence. In addition, the scanner was overhauled 10 years after installation, when the 22 out of 448 detector blocks were replaced and the linear and energy correction tables of whole detectors were adjusted.

In the present study, we evaluated the performance of this PET scanner in terms of sensitivity, spatial resolution, and scatter and random coincidence fraction, and estimated the aging effects on these performances.

Sensitivity

In the present study, CCF measurement data were used for the retrospective evaluation of scanner sensitivity. For CCF measurements, we placed the cylindrical phantom (20-cm in inner diameter, 25-cm in length), which was filled with [^{18}F] water solution (30.6–11.1 MBq, average of 19.6 MBq), at the center of the effective FOV, and emission data were obtained for 10–30 min in 2D mode. The activity in the phantom was determined by measuring the total amount of activity injected into the phantom by a calibrated dose calibrator. The lower energy threshold was set at 292 ch. The coincidence rate at the starting time of measurement for all sinograms was calculated on the basis of the data corrected for random coincidences, dead time and decay; scanner sensitivity was calculated as the count rate per unit activity concentration (Bq/ml). We examined the changes in sensitivity caused by aging on the basis of previous CCF measurement data obtained in 2D mode during the period only from 5 to 13 years after the time of installation of the scanner (data for 1–4 years after installation were lost and could not be included). In addition, the sensitivity values for each slice were examined before and after the overhaul at 10 years after installation. The initial sensitivity of the scanner was as reported previously [10], which was measured according to the National Electrical Manufacturers Association (NEMA) NU2-1994 procedure [17]. We also measured the sensitivity of the scanner using the NEMA NU2-1994 procedure before and after the overhaul.

Spatial resolution

We measured the spatial resolution in trans-axial slices using a Teflon tube (inner diameter 0.5 mm) filled with [^{18}F] water solution of 2–9 MBq inserted into a stainless steel tube (outer diameter 3 mm, length 50 cm) as the radiation source. The emission scan of the line source by 2D mode was performed at 5 positions—0, 5, 10, 15, and 20 cm from the center of the FOV in a horizontal direction. The trans-axial images of the source were reconstructed using the filtered back-projection method with a ramp filter. A count profile curve of the source image was generated; this was used to calculate the values of full width at half-maximum (FWHM) and full width at tenth-maximum (FWTM). We calculated the mean values of FWHM and FWTM across the slices, as well as the standard deviation. The measurements of spatial resolution for trans-axial slices were performed at the time of installation, 8 years after installation, and immediately after the overhaul (10 years after installation).

Scatter fraction variation

We also examined the variation in the ratio of the scatter coincidence to the true plus scatter coincidence. The 63 sinograms of the CCF measurement data were merged into a single sinogram for each measurement. We defined the values detected in the region of interest (ROI_{S+T}) placed in the phantom region as the true and the scattered coincidences, whereas the values detected in the ROI out of the phantom region (ROI_S) were regarded as scattered coincidences, as shown in Fig. 2. The size and location of these ROIs were fixed for all merged sinogram data. A ratio of the mean of ROI_S to the mean of ROI_{S+T} was calculated for each sinogram; we defined this as "tentative scatter fraction". The tentative scatter fraction variation was calculated using data in the period between 5 and 13 years

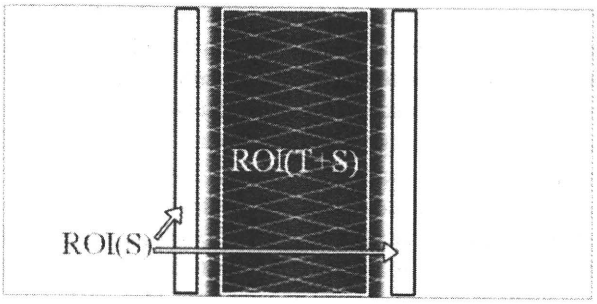

Fig. 2 Size and location of the ROIs used for evaluating the scatter fraction

after installation. In addition, we conducted two experiments to confirm the effectiveness of the tentative scatter fraction. One experiment assessed the tentative scatter fraction variation by CCF measurement, as mentioned above, and the other experiment assessed the system scatter fraction measurements according to the NEMA NU 2-2001 protocol [18]. The NEMA protocol has commonly been used in the past to evaluate the scatter fraction of PET scanners [11, 12]. These experiments were performed with a change in energy threshold level from channel (not corresponding to keV) 100–500 in 2D mode. The NEMA scatter measurement uses a NEMA scatter phantom (20-cm diameter and 70-cm long solid polyethylene cylinder) to which a 70-cm long line source filled with low activity of [^{18}F] water solution was inserted at a 4.5 cm radial offset from the center of the phantom. Although data should be acquired at a random rate below 1.0% of the true rate in the NEMA scatter fraction measurements, we could not satisfy this using our measurements. Therefore, prompt minus random counts were measured. The counts within a 24-cm transverse FOV were used to determine the true and scattered coincidence counts for the calculations of system scatter fraction. Relative values of the tentative and the system scatter fraction were obtained by dividing the individual fraction by the fraction at 100 ch threshold in each data set; these data were compared as a function of the threshold level.

Random coincidence fraction

We used the ratio of random coincidence fraction to prompt coincidence rate as an index of the scanner coincidence characteristics. Regarding the evaluation of random coincidence, we measured the prompt coincidence rate and the random coincidence rate before and after the overhaul relative to a given radioactivity value, using a cylinder phantom. We filled the cylinder phantom used in the measurement of sensitivity with [^{18}F] water solution (740 MBq) in order to measure the prompt coincidence rate and the random coincidence rate in 2D mode until the

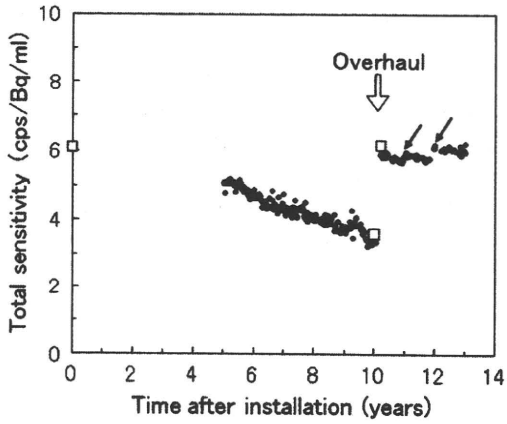

Fig. 3 Variation in sensitivity of PET scanners over time, where closed circles and open squares indicate the sensitivity as assessed using CCF measurement and the NEMA protocol, respectively. NEMA sensitivities were measured at the time when the scanner was installed, and before and after the overhaul. The total count rate indicated an overall reduction of 41% in the 10 years before the overhaul. After the overhaul, the sensitivity was restored to up to almost the initial value. Slight increases in sensitivity corresponded to the replacement of cooling fans, which was also observed at 1 and 2 years after the overhaul (*black arrows*)

radioactivity decayed to near the background level. The random coincidence rate fraction against the random coincidence rate was compared before and after the overhaul.

Results

Sensitivity

The results of the sensitivity changes in CCF measurement data (closed circles) from 5 to 13 years after installation and in the NEMA measurement data (open squares) are shown in Fig. 3. The sensitivity at the time of installation (time 0) was 6.1 cps/Bq/ml [10]; this decreased almost linearly from time 0 to 10 years after installation, although there were no CCF measurement data between time 0 and 5 years. The total reduction of the sensitivity over 10 years was 41% using the NEMA measurement system and the mean reduction rate obtained from CCF measurements was 4.7% per year until the time of the overhaul. At the same time, dose calibrator stability, as assessed by measurement of the long-life standard source, stayed constant (data not presented here). After the overhaul, the sensitivity was restored to almost the same as the initial value (Fig. 3). Figure 3 also shows that sensitivities assessed by CCF measurement before and after the overhaul agreed well with the sensitivities assessed by NEMA measurement. Interestingly, slight increases in sensitivity occurred after 1

and 2 years after the overhaul (11 and 12 years elapsed), and then the sensitivity decreased slowly after each increasing year (black arrows in Fig. 3). As a result, a notable reduction in sensitivity was not observed during the first 3 years after the overhaul. Figure 4 shows the relative slice sensitivity variation of before (closed circles) and after (open circles) the overhaul as mean slice sensitivity of each measurement; the dashed line in the graph indicates a border of detector block ring. Regarding the sensitivity with respect to each slice, there was a tendency for inter-slice variation to increase in sensitivity before the overhaul.

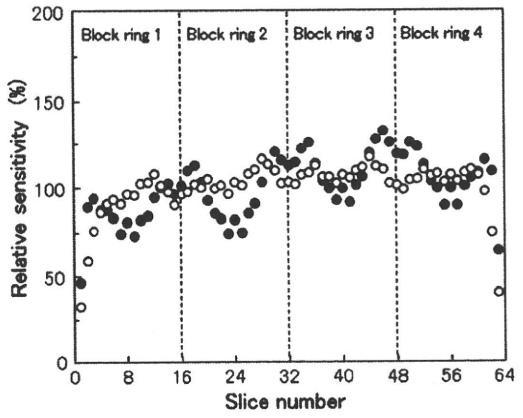

Fig. 4 Variation in slice sensitivity before and after the overhaul, where *closed circles* indicate the sensitivity before the overhaul and *open circles* indicate sensitivity after the overhaul. The *dashed line* in the graph indicates a border of detector block ring. There is a tendency for inter-slice variation to increase in the sensitivity before the overhaul

The variation in the slice sensitivity before the overhaul tended to be lower around slices at the center of the block ring and higher around slices at the marginal areas when compared with the variation after the overhaul.

Spatial resolution

The FWHM and the FWTM values corresponding to 1, 8, and 10 years after the installation are shown in Table 2. In year 8, a slight increase in FWHM and FWTM values was detected (Table 2). However, the average rates of increase in FWHM and FWTM values were 1.7 and 3.6%, respectively. This reduction of the spatial resolution was restored to the original values with a deviation of 0.5 and 1.5%, respectively (Table 2).

Scatter fraction variation and random fraction

The tentative scatter fraction dropped from 4.7 to 4.1% during the 5 years prior to the overhaul. In addition, after the overhaul, the scatter fraction increased from 4.1 to 5.1%; a slight increase and a slow decrease in scatter fraction could be recognized during the following 3 years (Fig. 5). The tentative scatter fraction variation showed a similar pattern of sensitivity variation. The relative change in the tentative and NEMA system scatter fraction as a function of the threshold level is shown in Fig. 6, where the values of the tentative and NEMA system scatter fraction were in good agreement. It was confirmed that the tentative scatter fraction correlated well with the variation in system scatter fraction and is a useful measure as a substitute for the system scatter fraction. The random fraction decreased

Table 2 Changes in spatial resolutions over time

Year	Distance from FOV center (cm)	FWHM (mm)		FWTM (mm)	
		Radial	Tangential	Radial	Tangential
1st (0)	0	4.4 ± 0.1	4.4 ± 0.1	8.9 ± 0.3	8.9 ± 0.2
	5	4.7 ± 0.1	4.6 ± 0.1	9.2 ± 0.2	9.1 ± 0.3
	10	5.4 ± 0.1	4.7 ± 0.1	10.4 ± 0.4	9.2 ± 0.2
	15	6.8 ± 0.1	5.3 ± 0.1	12.9 ± 0.5	10.2 ± 0.3
	20	7.8 ± 0.2	5.4 ± 0.1	14.6 ± 0.5	10.3 ± 0.3
8th	0	4.5 ± 0.2	4.5 ± 0.2	9.1 ± 0.2	9.6 ± 0.4
	5	4.7 ± 0.1	4.7 ± 0.1	9.5 ± 0.2	9.7 ± 0.5
	10	5.4 ± 0.1	4.8 ± 0.1	10.6 ± 0.3	9.6 ± 0.2
	15	6.8 ± 0.1	5.4 ± 0.1	13.0 ± 0.3	10.5 ± 0.3
	20	8.0 ± 0.2	5.5 ± 0.1	15.2 ± 0.5	10.7 ± 0.3
10th (after overhaul)	0	4.4 ± 0.3	4.5 ± 0.2	9.0 ± 0.3	9.3 ± 0.4
	5	4.7 ± 0.1	4.6 ± 0.1	9.3 ± 0.2	9.2 ± 0.3
	10	5.3 ± 0.1	4.7 ± 0.1	10.4 ± 0.3	9.3 ± 0.2
	15	6.6 ± 0.1	5.2 ± 0.1	12.7 ± 0.3	10.3 ± 0.2
	20	7.7 ± 0.2	5.5 ± 0.1	14.8 ± 0.4	10.8 ± 0.3

FOV field of view, *FWHM* full width at half-maximum, *FWTM* full width at tenth-maximum

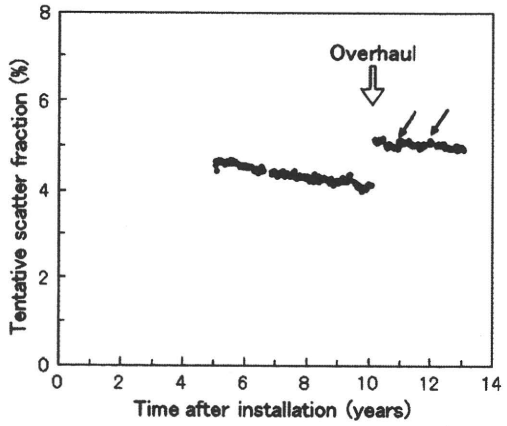

Fig. 5 Changes in the tentative scatter fraction. The scatter fraction decreased from 4.7 to 4.1% during the 5 years prior to the overhaul. The tentative scatter fraction increased significantly compared with that observed before the overhaul. Slight increases in scatter fraction corresponded to the replacement of cooling fans, which was observed at 1 and 2 years after the overhaul (*black arrows*)

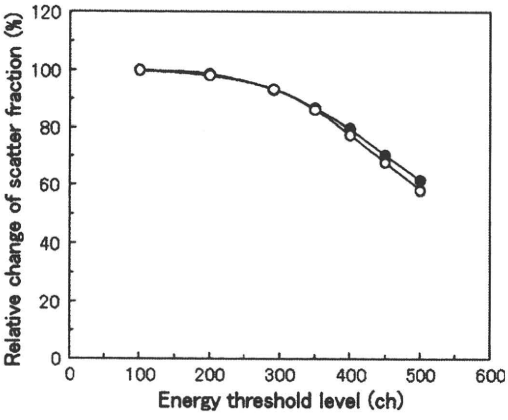

Fig. 6 Relative changes in the tentative scatter fraction and NEMA system scatter fraction as a function of the energy threshold level, where *open circles* indicate the tentative scatter fraction and *closed circles* indicate the NEMA system scatter fraction. In this diagram, the relative values of the scatter fraction were calculated (a value at 100 ch was assumed to be 100%). Good agreement was observed between the two values

by 10–15% after the overhaul within a range of random count rates ranging from 1 to 120 kcps (Fig. 7).

Discussion

In this report, we examined several important parameters associated with the performance of our PET scanner (SET-2400W). It is noteworthy that the sensitivity value decreased by 41% in 10 years (Fig. 3), which represents the largest change of all the parameters measured. In

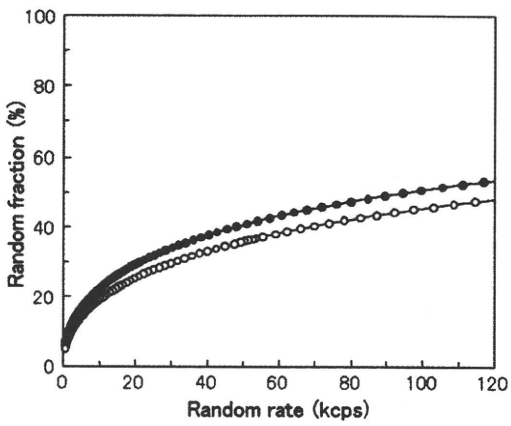

Fig. 7 The random fraction as a function of the random rate before (*closed circles*) and after (*open circles*) the overhaul

addition, scanner sensitivity was able to be evaluated by collection of CCF measurement data. In this regard, the sensitivity evaluation using the CCF measurement data is effective for monitoring performance changes of our PET scanners with aging. One of the main causes for the sensitivity reduction might be the reduction of PMT gain of the detectors, which results in a shift of the photopeak of the annihilation photons from the proper energy window. Previous observations, using other clinical PET scanners, have also indicated that the sensitivity was reduced as the years pass by [6, 15], and Uribe et al. [19] reported that PMT gain could drop by 11% systematically even over a period of 100 days. Therefore, proper PMT tuning is important in order to maintain the sensitivity of PET scanners. On the other hand, Zhang et al. [16] reported good performance stability after 6 years of use. However, their animal PET scanner has only 15 PMTs. Therefore, it is thought that overall PMT gain was tuned at regular maintenance times compared with human PET scanners, which had PMTs that ranged from several hundred to over a thousand. The sensitivity recovery after the overhaul can be attributed to replacement of the detectors and adjustment of the PMT gain. The fact that the number of replaced detectors ($n = 22$) was less than 5% of the total number of detectors suggests that the main cause for the recovery is likely to be the adjustment of the PMT gain. On the other hand, slight increases and slow decreases in the sensitivity could be recognized during the first 3 years after the overhaul (black arrows in Fig. 3). As a result, a notable reduction in sensitivity was not observed after the overhaul. We checked the maintenance records of the PET scanner and found that the signal processing board cabinet and gantry cooling fans of the PET scanner were replaced just before each increase, respectively. It is considered that these maintenances would yield shifts in photopeaks. In particular, the temperature of the detectors would be

dropped by replacing the gantry cooling fans, and the reduction in temperature causes an increase in scintillator light output [20] and then changes in PMT gain. This is consistent with previous reports in a clinical PET scanner [21, 22]. However, we could not evaluate sensitivity changes at the early stage of installation because the data from time 0 to 4 years after installation were lost. Therefore, we are not sure why sensitivity is more stable after the overhaul. Further evaluation is necessary to confirm the tendency of sensitivity change.

There was a slight deterioration in spatial resolution due to aging although it was minimal compared with that in sensitivity. This result is also consistent with our previous observations [6]. The main cause of deterioration in spatial resolution can be attributed to an unfavorable PMT signal balance, which induces a mismatch between the PMT output signals and the linear correction table, which would result in increased positioning errors. This is associated with the fact that the slice sensitivity differed in individual detector block ring units (Fig. 4). However, the deterioration in the trans-axial resolution was only small. The reason for this small deterioration is that the maximum mispositioning is 11.4 mm (half of the detector block size) in in-plane direction and will be less in practice regarding a block-type detector. Uribe et al. [19] also reported that an 11% PMT gain drift might marginally affect the decoding accuracy for the 7×7 BGO array. Although there was a gain in PMT from the initial value on our PET scanner, the PMT gain shift after 10 years did not significantly affect the image resolution. Furthermore, regarding the reduction of the scatter fraction due to aging, the cause is thought to be due to the decreased rate of Compton scattering induced by the shift of the annihilation photon photo peak to a lower energy, thereby energy threshold level was increased. The shift can be induced by a decrease in PMT gain. The tentative scatter fraction variation (Fig. 5) showed a similar pattern of sensitivity variation (Fig. 3). This result supports the hypothesis that the cause of sensitivity variation was the PMT gain variation. Although the scatter fraction used in the present study is different from that mentioned in the NEMA standard, it is essential that the measurement is able to detect the change in performance from the initial state in performance monitoring. The present observation in Fig. 6 suggests that the alteration of the scatter fraction can act as an indicator of the changes in the ratio of the scatter coincidences to the true coincidences. The increase in the random coincidence fraction (Fig. 7) is thought to be caused by deterioration of the timing adjusting function for the coincidence, which is also caused by aging.

In the present study, we noted that an adjustment of the PMT gain has been performed regularly as part of the scheduled maintenance once every 6 months. However, the sensitivity recovered after the overhaul rather than after each scheduled maintenance procedure, which would suggest that adequate position and energy table is important for good sensitivity performance, in addition to appropriate gain. It could be additionally suggested that, therefore, the scheduled maintenance was not capable of recovering the gain of all detectors due to aging effects. However, the present observation indicates that the target PET scanner manifests high durability of more than 10 years with the aid of appropriate maintenance; without maintenance, its performance can deteriorate considerably.

There are standard norms for performance evaluation such as NEMA NU 2-2001 and the Japanese Engineering Standards of Radiological Apparatus X-73*A-2005 [23]. However, there are disadvantageous aspects in these norms, such as the complexity of the measurements and the need for an exclusive phantom for the measurements. The performance in sensitivity showed the largest deterioration in the present study. The cause of the change is thought to be the deterioration in PMT gain, although changes in the PMT gain can cause other kinds of performance deterioration, as investigated in this study. Random coincidence fraction is closely related to sensitivity. The random fraction increases because an improper setting of coincidence timing decreases the true coincidence rate but does not decrease the random coincidence rate. However, the coincidence timing is affected by not only PMT gain shift but also the adjustment of the detector pair in the coincidence-timing window. In this regard, although the sensitivity variation includes accuracy of coincidence timing, we assume that the random fraction should also be monitored periodically. These findings suggest that the best way to detect early performance deterioration is to monitor the sensitivity and random fraction, which cannot be restored through scheduled maintenance for our PET scanner. In addition, the merits of this method are that we can calculate the sensitivity and scatter fraction using CCF measurement data—data which are needed for the routine maintenance of the PET scanner—and extra time is not needed for additional measurements. In addition, the random fraction can be assessed using the same phantom as that used in the CCF measurements or may be assessed by CCF measurements if random coincidence can be recorded. It is recommended that the variation in the sensitivity based on the CCF measurement data or the random fraction is observed, and when deterioration is detected, a standard measurement is conducted.

One limitation of the present study is that we did not measure the image contrast, which is included in the NEMA NU-2 2001 standards. The relationship between these parameters and other parameters should be examined further.